

Mn²⁺/Sb³⁺ codoped luminescent metal halides in ratiometric optical fiber for multiparameter collaborative sensing

Yuzhen Wang,¹ Jiance Jin,² and Zhiguo Xia^{1,2,*}

¹ School of Physics and Optoelectronics, South China University of Technology, Guangzhou, 510641, China

² The State Key Laboratory of Luminescent Materials and Devices, Guangdong Provincial Key Laboratory of Fiber Laser Materials and Applied Techniques, Guangdong Engineering Technology Research and Development Center of Special Optical Fiber Materials and Devices, School of Materials Science and Engineering, South China University of Technology, Guangzhou 510641, China

(Received 2 March 2024; revised 2 April 2024; accepted 31 May 2024; published 24 June 2024)

Multifunctional integrated optical sensors have attracted considerable attention for their fast response and high precision. However, it remains a challenge to decouple the crosstalk on the multisensory in a single sensor to enhance reliability and practicality. Here, we present a generic strategy for introducing multiple optical parameters, a fluorescence intensity ratio, and a lifetime to monitor alterations of temperature and strain synergistically. An ultrasensitive sensing platform with suitable multiple emissions was constructed by designing luminescent metal halides to realize versatile energy transfer channels between intrinsic self-trapped excitons and dopants' emission centers. Thus, the flexible fiber was fabricated and committed to monitoring temperature and strain in real-time working conditions with precision and repeatability. Moreover, the decoupling of temperature and strain sensing can be performed by the fluorescence intensity ratio and the lifetime of the Mn²⁺ ions. This work paves the way for emerging luminescent metal halides with multiple emissions applied in advanced multifunctional optical sensors and provides the solution for decoupling the crosstalk on the multisensory to enhance its reliability and practicality.

DOI: 10.1103/PhysRevApplied.21.064054

I. INTRODUCTION

Optical sensors based on light-matter interactions demonstrate enormous potential for detecting pH [1], stress [2], oxygen [3], and temperature [4,5] since they possess excellent merits including fast response, dynamically adaptive, and robust resistance to electromagnetic interference. Concretely, the optical sensors are conducted by decoding the functional relation between the target properties (the temperature and strain) and luminescence properties (the intensity, intensity ratio, lifetime, bandwidth, spectral shift, and polarization) [6]. Therein, the fluorescence intensity ratio (FIR) method is executed by dividing the intensities of two emissions, which has been widely reported [7,8]. Notably, the fundamental requirement for the fluorescence intensity ratio method is multiple emissions in light-emitting materials, which can be achieved by emerging ion-doped zero-dimensional (0D) luminescent metal halides (LMHs). Usually, flexible films based on 0D LMHs have been successfully explored via low-cost, large-scale, and facile synthesis. Nevertheless, they are

predominantly devoted to anticounterfeiting and imaging while scarcely applied in sensing [9–11].

Typically, 0D LMHs are composed of cations in an A site (Cs⁺, Rb⁺, K⁺, and large organic cations) and B sites with the halide ions (Cl⁻, Br⁻, I⁻) in X sites [12]. Strikingly, 0D LMHs have attracted considerable attention owing to their distinctive structures and regulable luminescence properties [13], and B-site cations constitute polyhedrons with halide ions and predominantly determine the luminescence performance [13,14]. Admittedly, the luminescence in 0D LMHs results from the delocalized ultrasmall Frenkel-like self-trapped excitons (STEs) induced by Jahn-Teller distortions in the crystals [15–17]. When stimulated by excitation light, strong electron-phonon coupling effects give rise to transient lattice distortion, then the resultant traps capture the photogenerated electrons and eventually release energy with tunable emissions [18]. Moreover, it is noteworthy that the luminescence properties of 0D LMHs can be regulated by introducing dopant ions (Mn²⁺, Sb³⁺, Bi³⁺, Te⁴⁺), and the impurities generate new energy levels, including extrinsic STE emissions and/or ionic luminescence [19,20]. Therefore, the emissions of 0D LMHs can be modified from ultraviolet to red or even near-infrared regions assisted by the

*Contact author: xiazg@scut.edu.cn

multiple emissions from STEs and impurities or energy transfer between different excited states [19,21–23].

In this regard, 0D LMH $\text{Rb}_3\text{KCdCl}_6:\text{Mn}^{2+}/\text{Sb}^{3+}$ crystals have been designed and prepared herein, which display two distinct emissions derived from extrinsic STEs of Sb^{3+} (518 nm) and $d-d$ transition of Mn^{2+} (605 nm) under excitation at 340 nm. The intrinsic reasons accounting for the difference in luminescence properties of STEs and ionic impurities were carefully investigated. Moreover, the tunable emission colors from green to orange can be manipulated by varying the concentration of Mn^{2+} and temperature. More importantly, in view of the various responses of two emissions in $\text{Rb}_3\text{KCdCl}_6:\text{Mn}/\text{Sb}$ crystals to temperature, the FIR method can be employed to monitor the alterations. The as-prepared stretchable optical fibers based on $\text{Rb}_3\text{KCdCl}_6:\text{Mn}/\text{Sb}$ crystals and polydimethylsiloxane (PDMS) were capable of detecting the temperature and strain with outstanding precision and repeatability. Nevertheless, the temperature and strain sensing are always executed when either is strictly restricted. The optical fiber generally transduces various stimuli into coupled signals (FIR), leading to a significant dilemma for discriminating specific inducements. Given the dimension of the solution, space should be no less favorable than the number of variables. It is essential to introduce other parameters for decoupling the multisensory. Fortunately, the delicate 0D structure preserves the long decay time of Mn^{2+} for tens of milliseconds, which is temperature-dependent and strain-independent, demonstrating a curative effect for discerning temperature and strain. As a result, we construct a decoupled matrix to bridge temperature and strain with FIR and decay time of Mn^{2+} , which naturally realizes the multifunctional sensing based on the single optical platform.

II. EXPERIMENTAL AND COMPUTATIONAL DETAILS

The reagents are Rb_2CO_3 (99.9%, Macklin), K_2CO_3 (99%, Aladdin), CdCO_3 (98%, Macklin), $\text{Sb}(\text{CH}_3\text{COO})_3$ (97%, Macklin), MnCl_2 (99.9%, Aladdin), HCl aqueous solution (Sinopharm Chemical Reagent Co., Ltd., China), N,N-dimethylformamide (DMF, 99.5%, Shanghai RichJoint Chemical Reagents Co., Ltd.), and anhydrous ethanol (99.5%, Shanghai RichJoint Chemical Reagents Co., Ltd.). All the chemicals were utilized without further purification. The $\text{Rb}_3\text{KCdCl}_6:0.2\text{Sb}$ crystals doped with 0, 0.05, 0.1, 0.2, and 0.3 Mn were synthesized by a modified solution method. Firstly, the raw material powders (carbonates, antimony acetate, and manganese chloride anhydrous) were carefully weighed according to stoichiometric ratio to prepare a 1-mmol product, and then were placed in a 20-ml glass bottle. Afterward, 3-ml HCl aqueous solution and DMF were successively poured into the bottle while intense stirring was undertaken. Subsequently,

the mixture was heated to 100 °C, and a homogeneous colorless solution was obtained. Unlike the ordinary natural cooling process, we used an ice bath to obtain the solution to prevent the growth of crystals. Then, 3 ml of anhydrous ethanol was added to the cold solution to demolish its steady state. Instantly, the crystals precipitated and the solution became a turbid liquid. Hereupon, centrifugal cleaning of the crystals was performed several times with anhydrous ethanol, and then it was dried in the oven at 60 °C.

The $\text{Rb}_3\text{KCdCl}_6:0.2\text{Sb}/0.05\text{Mn}$ (CSM) flexible optical fiber was prepared by a modeling method. A quantity of 5 ml of PDMS (10:1 mixing ratio) along with 0.5 g of CSM crystal powders were stirred to obtain a colloidal mixture. After degassing under vacuum, the mixture was injected into a hollow plastic tube with two silica fibers inserted into the end as a “Y” type fiber core. After solidification, the plastic pipe was stripped and the core of the optical fiber was poised. Furthermore, the cladding is composed of PDMS. After dipped into the PDMS, the coated core rotated at high speed to form a homogeneous cladding and then heated at 100 °C for solidification.

The CSM flexible optical film was also fabricated using a modeling method. A quantity of 10 ml of PDMS (10:1 mixing ratio) along with 1 g of CSM crystals were stirred to produce a colloidal mixture, and then poured into a Teflon container with a side length of 10 cm and a depth of 2 mm. Finally, the mixture was heated at 100 °C for solidification.

The x-ray diffraction patterns were measured at room temperature using a D8 Advance diffractometer with $\text{Cu K}\alpha$ ($\lambda = 1.541862 \text{ \AA}$) radiation operating at 40 kV and 40 mA. Scanning electron microscope images and element mappings were obtained by using a JSM-7900 F scanning electron microscope with an electron dispersive spectrometer. X-ray photoelectron spectroscopy was measured by a ThermoFisher Nexsa x-ray photoelectron spectroscopy instrument. The photoluminescence excitation (PLE), photoluminescence (PL) spectra, and PL decay curves of the samples were detected by an Edinburgh Instruments FLS1000 fluorescence spectrophotometer equipped with a xenon lamp (operating at 450 W) as the excitation source. The temperature-dependent PL spectra were collected using the same spectrophotometer that was equipped with cryogenic liquid nitrogen plant equipment. Also, the same equipment assembled a 340-nm laser as the light source to avoid interference from the lifespan of the xenon lamps, which was employed to detect the decay times under various temperatures. In addition, the luminescence and decay time of the as-fabricated optical fiber under various temperatures and strains was recorded by a fiber optic spectrometer (QE Pro, Ocean Optics) equipped with a pulse frequency modulator and a 375-nm laser, and real-time data was recorded and analyzed by the software OCEANVIEW 1.6.3. Moreover, the morphologies of the

CSM optical fiber were obtained by an optical microscope (Zeiss Imager Z2).

The density functional theory (DFT) calculations for Rb₃KCdCl₆, Rb₃KCd_{0.8}Sb_{0.2}Cl₆, Rb₃KCd_{0.95}Mn_{0.05}Cl₆, and Rb₃KCd_{0.75}Sb_{0.2}Mn_{0.05}Cl₆ was performed by the VIENNA AB INITIO SIMULATION PACKAGE. The projector-augmented wave method based on a generalized gradient approximation was employed, and the exchange-correlation potential was presented via the Perdew-Burke-Ernzerhof format. During the calculations, the supercells were constructed with a cutoff energy of 380 eV, the electronic iteration convergence was 10⁻⁵ eV, and the atoms were fully relaxed until the Hellmann-Feynman forces reached 0.01 eV/Å.

The formation energy E_f for Sb³⁺ and/or Mn²⁺ doped in Rb₃KCdCl₆ crystals were calculated via:

$$E_f = E_{\text{doped}} - E_{\text{undoped}} - \sum n_i \mu_i \quad (1)$$

where E_{doped} and E_{undoped} denote the total energy of the supercells with the presence and absence of impurities (Sb³⁺, Mn²⁺), respectively. Moreover, n_i and μ_i refer to the number of added ($n_i > 0$) or removed ($n_i < 0$) i -type atoms and the corresponding chemical potentials, respectively.

III. STRUCTURE ANALYSIS

As displayed in Fig. 1(a), Rb and K with large radius isolate [CdCl₆] octahedrons in the 0D Rb₃KCdCl₆ lattice. The crystal is subjected to the trigonal system with a space group of R3c (No. 167). Notably, nominal Rb₃KCdCl₆:0.2Sb³⁺ crystals doped with various concentrations of Mn²⁺ were fabricated by a modified solution method (illustrated in Fig. S1 in the Supplemental Material and the Experimental section) [24], and the corresponding pure phases were confirmed by x-ray diffraction patterns and depicted in Fig. S2(a) in the Supplemental Material [24]. After the dissolving of the precursors in hydrochloric acid and hydrophobic solvent (N, N-Dimethylformamide, DMF), the transparent solution underwent cooling via an ice bath to inhibit the nucleation of crystals, giving rise to relatively uniform particles. Due to the similar ionic radius, Sb³⁺ (0.76 Å) and Mn²⁺ (0.83 Å) occupy Cd²⁺ (0.95 Å) sites as [SbCl₆]/[MnCl₆] in crystalline form. Different from Mn²⁺ ions doping, the Sb³⁺ ions nonequivalently substitute Cd²⁺ ions, resulting in a monovalent vacancy. According to the formation energy E_f values via first-principle density functional theory calculations, the monovalent vacancy is testified to be K⁺ vacancy, as displayed in Table S1 in the Supplemental Material [24]. Figure S2(b) in the Supplemental Material [24] presents the Rb₃KCdCl₆:0.2Sb/0.05Mn crystals in regular shape, and the side length is about tens of micrometers. In addition, the element mappings of Rb, K, Cd, Cl, Sb, and Mn illustrate their uniform distribution in the crystals, and

the conspicuous signals of Sb and Mn in x-ray photoelectron spectroscopy demonstrate the successful introduction of Sb and Mn ions into the crystal [Figs. S2(c) and S2(d) in the Supplemental Material] [24]. Furthermore, the DFT calculation unveils the electronic structures of the Rb₃KCdCl₆ matrix, Rb₃KCdCl₆:0.05Mn, Rb₃KCdCl₆:0.2Sb, and Rb₃KCdCl₆:0.2Sb/0.05Mn samples, and the band structures, corresponding to the density of states (DOS) of each element and total DOS, are also obtained (Fig. S3 in the Supplemental Material) [24]. Obviously, the direct band gap remains located at the L -point in the Brillouin zone while the value dwindle, which is induced by the dopants. In CSM crystals, the [SbCl₆] and [MnCl₆] contribute to the conduction band minimum (CBM) and valence band maximum (VBM), respectively. Specifically, the 4d orbital of Mn²⁺ and 5s orbital of Sb³⁺ form the interstitial states between CBM and VBM, which suggests a possible energy transfer process for luminescence.

IV. PHOTOLUMINESCENCE PROPERTIES

To experimentally determine the luminescence properties, we monitored the photoluminescence (PL) and PL excitation (PLE) spectra of the CSM crystals at room temperature [shown in Fig. 1(b)]. Apparently, the two distinctive luminescence centers stem from extrinsic STEs induced by Sb³⁺ and the spin-forbidden $^4T_1 \rightarrow ^6A_1$ transition of six coordinated Mn²⁺. Moreover, the excitation bands in the PLE spectra of extrinsic STEs and Mn²⁺ luminescence show no distinction from 250 to 400 nm, indicating a possible energy transfer process in the CSM crystals. Notably, the characteristic sharp peaks assigned to the Mn²⁺ ions are absent in the PLE spectra, implying that the population on the excited state 4T_1 of Mn²⁺ is achieved by energy transfer from the excited state of extrinsic STEs and nonradiative relaxation from the valence band of Rb₃KCdCl₆ host, which is consistent to the DFT calculation results. With increasing Mn²⁺ concentration, the emission intensity of the extrinsic STEs gradually decreases, while that of Mn²⁺ transitions progressively ascends, revealing the tunable emission color from green to orange [Fig. S4(a) in the Supplemental Material] [24]. According to the structural optimization conducted by the DFT calculation, the distance between Sb and Mn is 7.81 Å, which is too large to induce exchange interaction. Following Dexter's energy transfer expression for multipolar interactions and Reisfeld's approximation, the luminescence intensity of various concentration Mn²⁺-doped samples can be described as follows [25,26]:

$$\frac{I_{\text{Sb}}}{I_{\text{Sb-Mn}}} \propto C^{n/3}, \quad (2)$$

where C denotes the concentration of Mn²⁺, and I_{Sb} and $I_{\text{Sb-Mn}}$ represent the luminescence intensity of

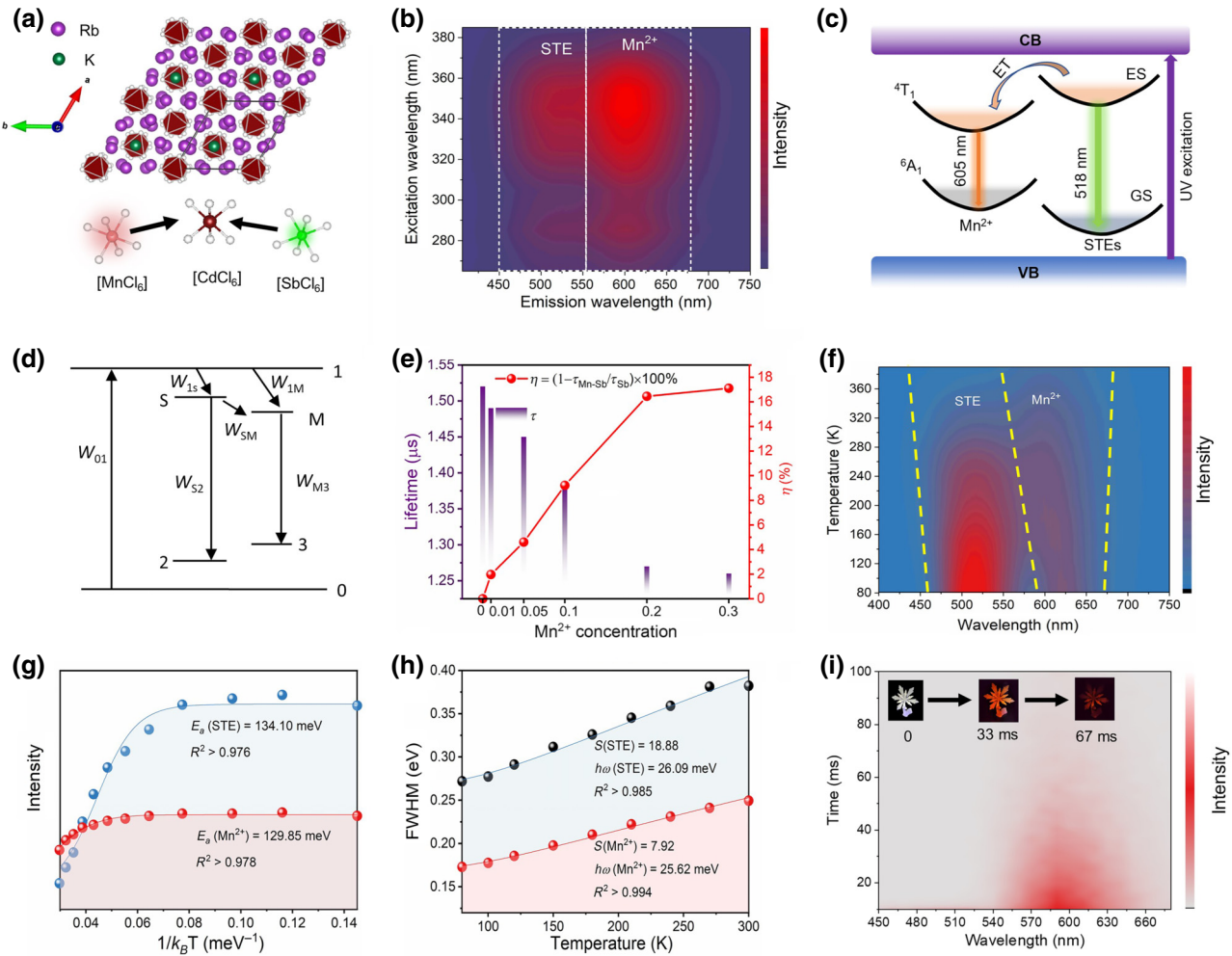


FIG. 1. Structure and photoluminescence of the CSM crystals. (a) Crystalline structure of $\text{Rb}_3\text{KCdCl}_6$ and schematic diagram of the Sb-Mn substitution. (b) Excitation and emission spectra of the CSM crystal. (c) Possible energy transition mechanism in the CSM crystal. (d) Simplified energy transfer mechanism for the CSM crystal. Here, 0 and 1 are the VB and CB of the host materials, respectively, and 2 and 3 refer to the ground state of the STEs and Mn²⁺, respectively. Moreover, S and M represent the excited states of the STEs and Mn²⁺, respectively. Furthermore, W_{ij} denotes the energy transfer rate from state i to state j . (e) Estimated decay times of various Mn²⁺-doped crystals and corresponding energy efficiency from the extrinsic STE to Mn²⁺ ions. (f) Temperature-dependent PL spectra of the CSM crystal excited by 340 nm. (g) Activation energy of the STE and Mn²⁺ in the form of an Arrhenius plot. (h) FWHM values of the STEs and Mn²⁺ emission peaks depending on temperature. (i) Time-resolved emission spectra of the CSM crystal. Insets are the luminescence photographs after stopping excitation for 0, 33, and 67 ms.

$\text{Rb}_3\text{KCdCl}_6:0.2\text{Sb}$ crystals with the absence and presence of Mn²⁺, respectively. More importantly, $n = 6, 8$, and 10 are related to dipole-dipole, dipole-quadrupole, and quadrupole-quadrupole interactions, respectively [25,26]. After fitting the intensity ratio curve with varying the concentration of Mn²⁺, as displayed in Figs. S4(c)–S4(e) in the Supplemental Material [24], n tends toward 6, indicating the dipole-dipole interaction induces energy transfer from the extrinsic STE and Mn²⁺. Furthermore, Fig. 1(c) illustrates the possible energy transition mechanism in $\text{Rb}_3\text{KCdCl}_6:\text{Sb}/\text{Mn}$ crystals. Under excitation by high-energy ultraviolet light, the electrons transverse to the conduction band (CB) from the valence band (VB) of the

host, then they are captured by the excited state (ES) of the extrinsic STEs and, eventually, are released to the ground state (GS), accompanied by a broadband green emission centered at 518 nm. The electron population on the $^4\text{T}_1$ energy level of the Mn²⁺ ions is from the CB, which partially originates from the energy transfer process from the extrinsic STEs and, subsequently, dissipates to the $^6\text{A}_1$ state with an emission of 605 nm.

To unveil the difference in luminescence intensities between the STEs and Mn²⁺ ions, the rate equations for the population on the ES and GS of the extrinsic STEs and Mn²⁺ are demonstrated based on the simplified energy transfer model in Fig. 1(d). The rate equations relating to

the excited states S and M can be summarized as [27,28]:

$$\frac{dN_S}{dt} = N_1 W_{1S} - N_S W_{S2} - N_S W_{SM}, \quad (3)$$

$$\frac{dN_M}{dt} = N_1 W_{1M} - N_M W_{M3} + N_S W_{SM}, \quad (4)$$

respectively, where N_i refers to the population density in state i . After solving the differential equations, the N_S and N_M are written as follows:

$$N_S = \frac{N_1 W_{1S}}{W_{S2} + W_{SM}} - \frac{1}{W_{S2} + W_{SM}} \times \exp[-(W_{S2} + W_{SM})t + C_1], \quad (5)$$

$$N_M = \frac{N_1 W_{1M} + N_S W_{SM}}{W_{M3}} - \frac{1}{W_{M3}} \exp(-W_{M3}t + C_2), \quad (6)$$

where C_1 and C_2 are constants. Under a steady-state excitation situation, the luminescence intensities of the STEs (denoted as I_{STE}) and Mn²⁺ ions, I_{Mn}^{2+} , are directly proportional to the population density in respective excited states. As a result, we find that

$$I_{\text{STE}} \propto N_S = \frac{N_1 W_{1S}}{W_{S2} + W_{SM}}, \quad (7)$$

$$I_{\text{Mn}^{2+}} \propto N_M = \frac{N_1 W_{1M} + N_S W_{SM}}{W_{M3}}. \quad (8)$$

According to Dexter's theory, the energy transfer rate w_{SM} of the dipole-dipole interaction can be expressed as [26]

$$w_{\text{SM}} = \frac{3}{64\pi^5} \frac{h^4 c^4}{\kappa^2 R^6} \frac{\sigma_M}{\tau_S} \int_0^\infty \frac{\varepsilon_S(h\nu) \alpha_M(h\nu)}{(h\nu)^4} dh\nu, \quad (9)$$

where h , c , κ , R , σ_M , τ_S , $\varepsilon_S(h\nu)$, and $\alpha_M(h\nu)$ represent the Planck constant, light velocity, permittivity, distance between Sb³⁺ and Mn²⁺, effective absorption cross-section, intrinsic lifetime of Sb³⁺, emission spectra, and absorption spectra, respectively. As a result, the energy transfer rate is inversely proportional to the lifetime of the extrinsic STEs. When the contents of Mn²⁺ increase from 0 to 0.3 in Rb₃KCdCl₆:0.2Sb crystals, the lifetime of the extrinsic STEs diminishes from 1.52 to 1.26 μs [Figs. 1(e) and S4(b) in the Supplemental Material [24]], indicating enhanced energy transfer from the extrinsic STEs to Mn²⁺ ions. The energy transfer efficiency η is defined as $\eta = 1 - \tau_{\text{Mn-Sb}}/\tau_{\text{Sb}}$, where $\tau_{\text{Mn-Sb}}$ and τ_{Sb} denote the lifetimes of Rb₃KCdCl₆:0.2Sb crystals with and without Mn co-doping, respectively [29]. Accordingly, the energy transfer from the STEs to the excited states of Mn²⁺ can be found, and it can reach 17.1% when introducing 0.3 Mn into the crystal, as shown in Fig. 1(e). Typically, according to the Struck and Fonger models, the declined lifetime

varying with temperature can be expressed as [30]

$$\tau(T) = \frac{\tau_0}{1 + A_1 \exp(-(\Delta E_a/k_B T))}, \quad (10)$$

where τ_0 , A_1 , ΔE_a , and k_B represent the initial lifetime, fitting factor, activation energy, and Boltzmann constant, respectively. Therefore, the energy transfer rate strongly correlates to the temperature and bridges the temperature and emission intensities of the extrinsic STE and Mn²⁺ ions. As a result, the different luminescence thermal quenching effects of the STEs and Mn²⁺ ions can be demonstrated, which is a fundamental of ratiometric optical thermometry in the present CSM crystals. The lifetime of the Sb³⁺ ions at various temperatures with the absence [Fig. S5(a) in the Supplemental Material] and presence [Fig. S5(b) in the Supplemental Material] of the Mn²⁺ ions doped in Rb₃KCdCl₆ single crystals were recorded, and the energy transfer efficiency gradually enhanced with elevating temperature [Fig. S5(c) in the Supplemental Material] [24].

Additionally, the tunable emission colors of the CSM crystal can be realized by varying temperatures. As exhibited in Fig. 1(f), the emission bands of the extrinsic STEs and Mn²⁺ emanate diverse tendencies with elevating temperatures from 81 to 390 K, and the luminescence color changes from green to orange. In particular, the extrinsic STEs maintain emission at 518 nm with a broadened full width at half maximum (FWHM). Nevertheless, when increasing the temperature, the Mn²⁺ emission shows a blueshift along with broad FWHM, which can be ascribed to the lattice expansion-induced narrowed $d-d$ splitting and a raised energy gap of the ${}^4T_1 \rightarrow {}^6A_1$ transition [21,31]. Generally, the activation energy E_a can be calculated via the integrated luminescence intensity $I(T)$ at T K, initial intensity I_0 , and Boltzmann constant k_B using the expression [4]:

$$I(T) = \frac{I_0}{1 + A \exp(-E_a/k_B T)} \quad (11)$$

where A is the fitting constant. Accordingly, the approximated activation energies of the extrinsic STEs and Mn²⁺ ions are formulated, see Fig. 1(g), and estimated to be 134.10 meV and 129.85 meV, respectively. Furthermore, the electron-phonon coupling is described by the Huang-Rays factor, S , following the formula [32]:

$$\text{FWHM}(T) = 2.36 \hbar \omega_{\text{phonon}} \sqrt{S \coth \left(\frac{\hbar \omega_{\text{phonon}}}{2k_B T} \right)}. \quad (12)$$

Here, $\hbar \omega_{\text{phonon}}$ represents the phonon energy; the values are 26.09 meV for the extrinsic STEs and 25.62 meV for the Mn²⁺ luminescence, suggesting a homogeneous lattice vibration in the CSM crystal. By contrast, the S

values reveal a significant difference between the extrinsic STEs (18.88) and Mn^{2+} (7.92), as depicted in Fig. 1(h), which indicates the distinction in their intrinsic luminescence mechanism. On the one hand, the appropriate strong electron-phonon coupling effect guarantees the materialization of the extrinsic STEs and facilitates luminescence [33]. On the other hand, the weak electron-phonon coupling effect influences the local symmetry of Mn^{2+} sites, which breaks the limitations of spin-forbidden transitions and leads to efficient red emissions from the CSM crystals. Considering similar E_a values, the prominently different S values portend the distinct luminescence thermal quenching performance of the STEs and Mn^{2+} ions. It is noteworthy that the subtle 0D structure of the LMH CSM crystals triggers the interesting luminescence properties of the Mn^{2+} ions. In line with the time-resolved emission spectrum of the CSM crystal [Fig. 1(i)], the green emission induced by the extrinsic STE exhibits rapid attenuation. In contrast, the red emission results from Mn^{2+} depict a long decay time. The inset luminescence photographs of Fig. 1(i) show the recorded red emission after stopping excitation for 0, 33, and 67 ms. Moreover, Fig. S6 in the Supplemental Material shows the prompt and delayed PL spectra of the CSM crystal under an excitation of 340 nm at room temperature, corroborating the long decay time of the Mn^{2+} ions. Fig. S7 in the Supplemental Material [24] displays the decay time of the Mn^{2+} ions monitored at 605 nm, decreasing from 52.1 ms to 21.5 ms with elevating temperature from 81 to 390 K. Such a long decay time can be attributed to the electronic transition of Mn^{2+} in isolated $[\text{MnCl}_6]$ octahedrons, induced by the spatially confined 0D structure of the $\text{Rb}_3\text{K}\text{CdCl}_6:\text{Sb}$ single crystal [21].

V. TEMPERATURE SENSING PROPERTIES

Given the diverse luminescence mechanism of the extrinsic STEs and Mn^{2+} ions, we calculated the emission intensity varying with temperature, as shown in Fig. S8(a) in the Supplemental Material [24]. With increasing temperature, the emission intensity of the extrinsic STEs and Mn^{2+} offers varying degrees of decrease. Theoretically, the energy-transfer-driven ratiometric thermometry can be implemented as Eqs. (6) and (7). The intensity ratio ($\text{FIR} = I_{\text{STE}}/I_{\text{Mn}^{2+}}$) is intuitively correlated to the energy transfer rate, temperature, and activation energy of the extrinsic STE and Mn^{2+} ions. Equation (S2) in the Supplemental Material [24] simply summarizes the functional relationship of FIR varying with temperature. Furthermore, Fig. S9 in the Supplemental Material [24] compares the theoretical results with experimental data, confirming the feasibility of the energy-transfer-driven ratiometric thermometry based on the 0D CSM single crystal. In addition, the FIR values varying with temperature can be phenomenologically effectively fitted by a cubic polynomial function with

$R^2 > 0.997$, as presented in Fig. S8(b) in the Supplemental Material [24]. Therefore, the temperature sensing performance herein is assessed by the absolute sensitivity S_A , relative sensitivity S_R , and temperature uncertainty δT , which are defined as follows [4,28]:

$$S_A = \frac{|d\text{FIR}|}{dT}, \quad (13)$$

$$S_R = \left| \frac{d\text{FIR}}{dT} \frac{1}{\text{FIR}} \right|, \quad (14)$$

$$\delta T = \frac{\delta\text{FIR}}{\text{FIR}} \frac{1}{S_R}, \quad (15)$$

Here,

$$\frac{\delta\text{FIR}}{\text{FIR}} = \sqrt{\left(\frac{\delta I_1}{I_1} \right)^2 + \left(\frac{\delta I_2}{I_2} \right)^2},$$

where $\delta I_{1,2}/I_{1,2}$ is the background intensity divided by the fluorescence intensity of the sample. Figure S8(c) in the Supplemental Material [24] displays the S_A and S_R values varying with temperature. The maximum S_A and S_R are 0.011 K^{-1} at 300 K and $5.22\% \text{ K}^{-1}$ at 390 K, respectively. In this work, the temperature-dependent PL spectra were detected by the Edinburgh Instruments FLS1000 fluorescence spectrophotometer, and the sample was placed into the temperature control accessory with liquid nitrogen cooling. In addition, the luminescence brightness of the CSM crystals is relatively high, contributing a considerable signal-to-noise ratio value. Moreover, $\delta\text{FIR}/\text{FIR}$ was estimated to be 0.03% after collecting the background and emission signals multiple times. The minimum δT is 0.006 K at 390 K (Fig. S10 in the Supplemental Material [24]). As compared in Fig. S8(d) in the Supplemental Material [24], the CSM crystals possess excellent potential for ratiometric optical thermometry [4,5,28,33–39].

Subsequently, the CSM crystals were adopted to fabricate stretchable optical sensors. The optical fiber was synthesized by mixing the CSM crystal powders into PDMS. The “Y” type stretchable optical fiber is composed of the core, cladding, and silica fibers. Specifically, the CSM crystals are conflated evenly in PDMS to form a fiber core with a diameter of 500 μm , and two silica fibers with diameters of 300 and 125 μm are inserted into the end for importing excitation light and exporting emission light. The attenuation of light is calculated for Fig. S11(a) in the Supplemental Material [24], and the propagation loss is 0.289 dB/cm. Moreover, the morphology of the core-cladding structure and particle dispersion are shown in Fig. S11(b) in the Supplemental Material [24]. During the measurements, the optical fiber stays relaxed to obviate the strain effect. As portrayed in Fig. 2(a), the as-fabricated flexible optical fiber maintains the same PL spectra as the CSM crystals, and the extrinsic STE emissions decrease while the ionic luminescence of Mn^{2+}

increases with an elevating temperature from 253 to 373 K. Figure 2(b) records the calibration curve of the FIR values changing with temperature. Afterward, we checked the accuracy of the as-fabricated optical fiber for temperature sensing through the contrast between the calculated results and the given temperature (measured by the thermocouple). Figure 2(c) unveils that the temperature measurement error is merely ± 0.2 °C at 28.2 °C after

hundreds of attempts, implying the preeminent reliability of the as-fabricated optical fiber for optical thermometry. Moreover, the fatigue resistance of the temperature sensing performance is demonstrated in Fig. S12 in the Supplemental Material [24]. After four cycles of heating and cooling, the FIR values display stable variation. Furthermore, we prepared squared flexible optical film based on the CSM crystals with a side length of 10 cm for

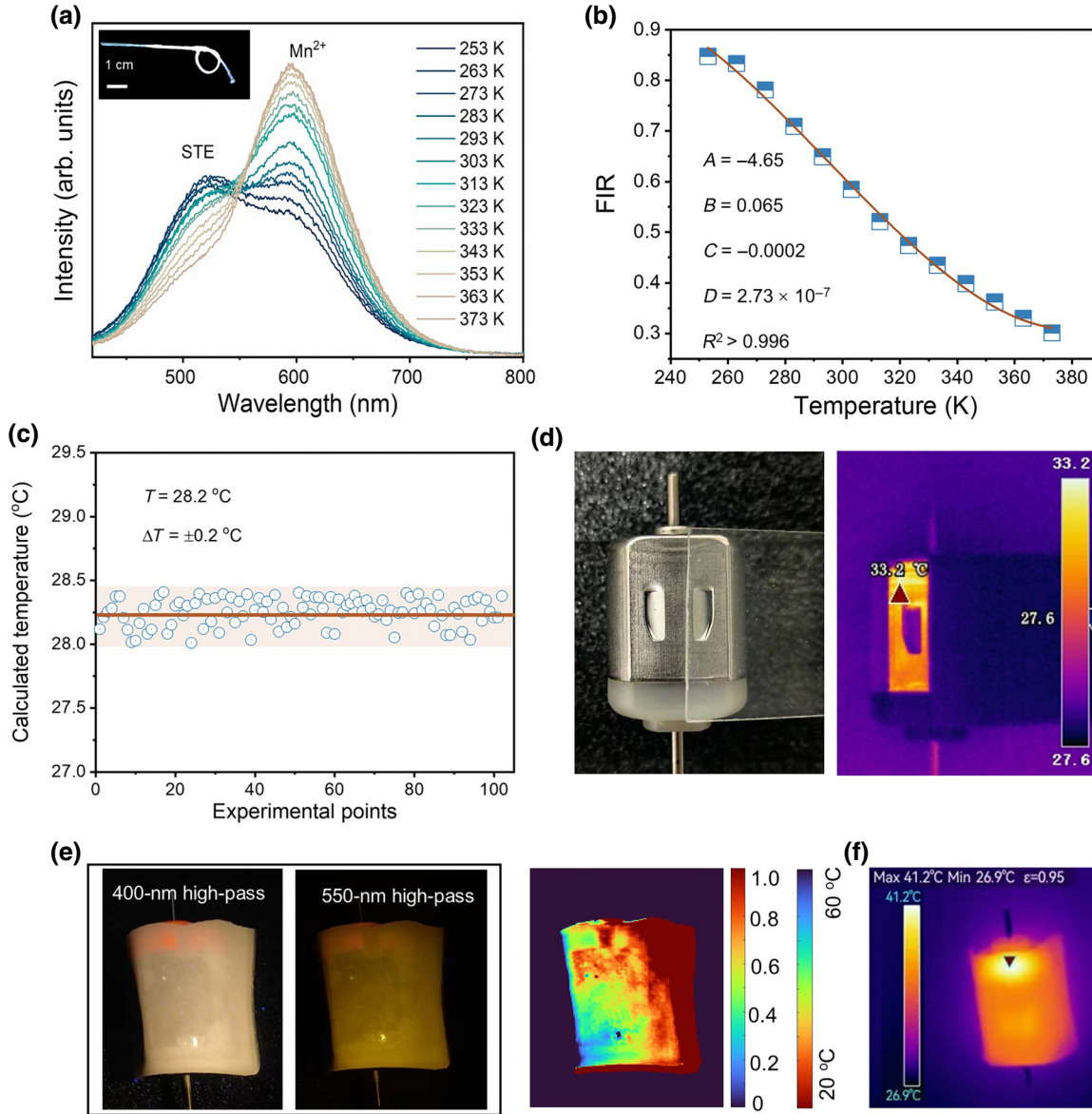


FIG. 2. Ratiometric temperature sensing of the CSM optical fiber and film. (a) Temperature-dependent PL spectra of the CSM optical fiber pumped by a 375-nm laser. The inset shows a photograph of an as-fabricated optical fiber. (b) Calibration curve of the CSM optical fiber and corresponding fitting function. (c) Temperature sensing accuracy at 28.2 °C. The factor ΔT is defined as the difference between temperatures measured by an as-fabricated optical fiber and a thermocouple. (d) Illustration of the unavailable thermal imaging of the object covered with a transparent glass plate by the IR thermal imager. (e) Luminescence photographs of the CSM optical film attached to the motor surface with 400- and 550-nm high-pass filters and calculated thermal imaging of the motor surface conducted by the CSM optical film based on the fluorescence intensity ratio method. (f) Thermal imaging of the motor surface with a CSM optical film captured by an IR camera.

thermal imaging, and the CSM crystals are evenly dispersed on the film [Figs. S11(d) and S13(a) in the Supplemental Material [24]]. It is noteworthy that the infrared (IR) camera cannot capture the temperature of targeted objects once hindered by a transparent glass plate [Fig. 2(d)]. However, luminescent thermal imaging based on the FIR approach can overcome this significant drawback. Remarkably, FIR-based thermal imaging is executed by deciphering the “V” value in the luminescence photographs in HSV format [40,41]. As demonstrated in Fig. 2(e), we attached the as-prepared film to the surface of the motor and took snapshots with 400- and 550-nm high-pass filters blocked in front of the camera under the same conditions. Specifically, luminescence pictures can be captured even at several meters away by a smartphone, indicating the practicability of remote thermal imaging via ratiometric optical thermometry. After extracting the data, the matrix concerning the emission intensity of total luminescence (the 400-nm high-pass filter) and the Mn²⁺ luminescence (the 550-nm high-pass filter) of each pixel point is obtained. The emission intensity of the extrinsic STEs is acquired by subtracting the value matrix of the Mn²⁺ luminescence from the total emissions. Subsequently, the FIR matrix of each pixel point is derived from the matrix division. Judging by the calibration data presented in Figs. S13(b)–S13(f) in the Supplemental Material [24], the theoretical temperature at each pixel can be converted by the FIR values. Figure 2(f) displays the thermal imaging of the motor surface, which is clearly consistent with the measurement results recorded by the commercial IR camera.

VI. STRAIN SENSING PROPERTIES

Interestingly, we further noticed that the FIR values positively correlate with the stretching of the CSM optical fiber at room temperature, implying its reasonable potential for strain sensing. The strain-dependent FIR may be attributed to the diverse transmission loss between green and red light. The strain ε is defined as dividing the initial length l ($l = 3$ cm in this work) into an extended length Δl , namely $\varepsilon = \Delta l/l$. And it denotes the relative change in length [42]. As presented in Fig. S14(a) in the Supplemental Material [24], the FIR value linearly decreases with increasing strain from 0 to 100%. Additionally, the CSM optical film for strain sensing unfolds stability after five cycles of stretching 0.5 and 2.0 cm [Fig. S14(b) in the Supplemental Material [24]].

VII. DECOUPLING OF MULTISENSORY

Accordingly, temperature and strain simultaneously affect the FIR values, leading to the dilemma of distinguishing temperature and strain solely based on the FIR method. Currently, multisensory functions are highly

desirable for applications in humanoid robotics, intelligent prosthetics, and human-machine interfaces [43,44]. However, the decoupling of multisensory properties is of great significance and has been an aporia all along [45]. In this context, we noticed that the lifetime of Mn²⁺ is tens of milliseconds, which can be devoted to temperature and strain sensing. As illustrated in Fig. 3(a), after setting the appropriate pulse width of the excitation source, the depopulation of STE and Mn²⁺ display diverse speeds. It is foreseeable that the PL decay of the Mn²⁺ ions could be delicately extracted once we choose a reasonable collection time. Figure 3(b) depicts the detailed measurement process. The frequency of the 375-nm laser was controlled by a pulse frequency modulator, and then the PL spectra were transported to the fiber optic spectrometer. Notably, the data collection time (i.e., the sum of the data update time and integration time) was strictly controlled so that the specific integral intensity decay of the red emission over time could be intuitively recorded by the fiber optic spectrometer. As shown in Fig. 3(c), the PL spectra at time t_0 , t_1 , and t_2 (and corresponding CSM optical fiber luminescence photographs) accurately meet the expectations. Furthermore, Figs. S15(a) and S15(b) in the Supplemental Material [24] depict the detailed experimental point of integral intensity (across 560–700 nm) in real time and the fitting results at 80 °C. Figs. S15(c) and S15(d) in Supplemental Material [24] present the corresponding photographs of the PL spectra at various annotated moments. The lifetime of the Mn²⁺ ions remains unchanged under different strains of the CSM optical fiber [Figs. 3(e) and S16 in the Supplemental Material [24]] and strongly correlates to temperature. Figures 3(d) and 3(e) summarized the FIR and lifetime $\tau_{\text{Mn}^{2+}}$ at various temperatures (30–100 °C) and strains (0–100%). Basically, the luminescence properties (luminescence intensity, lifetime, spectral shift, peak bandwidth, polarization, and FIR) show various responses to external conditions. As a result, we can construct a decoupling matrix composed of several functions, denoted by $f_{m,n}$, concatenating the luminescence properties Λ_1 , Λ_2 , ..., Λ_n and sensing performances X_1 , X_2 , ..., X_m as follows:

$$\begin{pmatrix} X_1 \\ X_2 \\ \vdots \\ X_m \end{pmatrix} = \begin{bmatrix} f_{1,1} & f_{2,1} & \cdots & f_{m,1} \\ f_{1,2} & f_{2,2} & \cdots & f_{m,2} \\ \vdots & \vdots & \ddots & \vdots \\ f_{1,n} & f_{2,n} & \cdots & f_{m,n} \end{bmatrix}^{-1} \begin{pmatrix} \Lambda_1 \\ \Lambda_2 \\ \vdots \\ \Lambda_n \end{pmatrix}. \quad (16)$$

In this work, the FIR and decay time of Mn²⁺ are introduced to decouple the temperature and strain sensing. The decoupling matrix can be established as [Fig. 3(f)]:

$$\begin{pmatrix} T \\ \varepsilon \end{pmatrix} = \begin{bmatrix} f_T & f_\varepsilon \\ g_T & g_\varepsilon \end{bmatrix}^{-1} \begin{pmatrix} \text{FIR} \\ \tau_{\text{Mn}^{2+}} \end{pmatrix}. \quad (17)$$

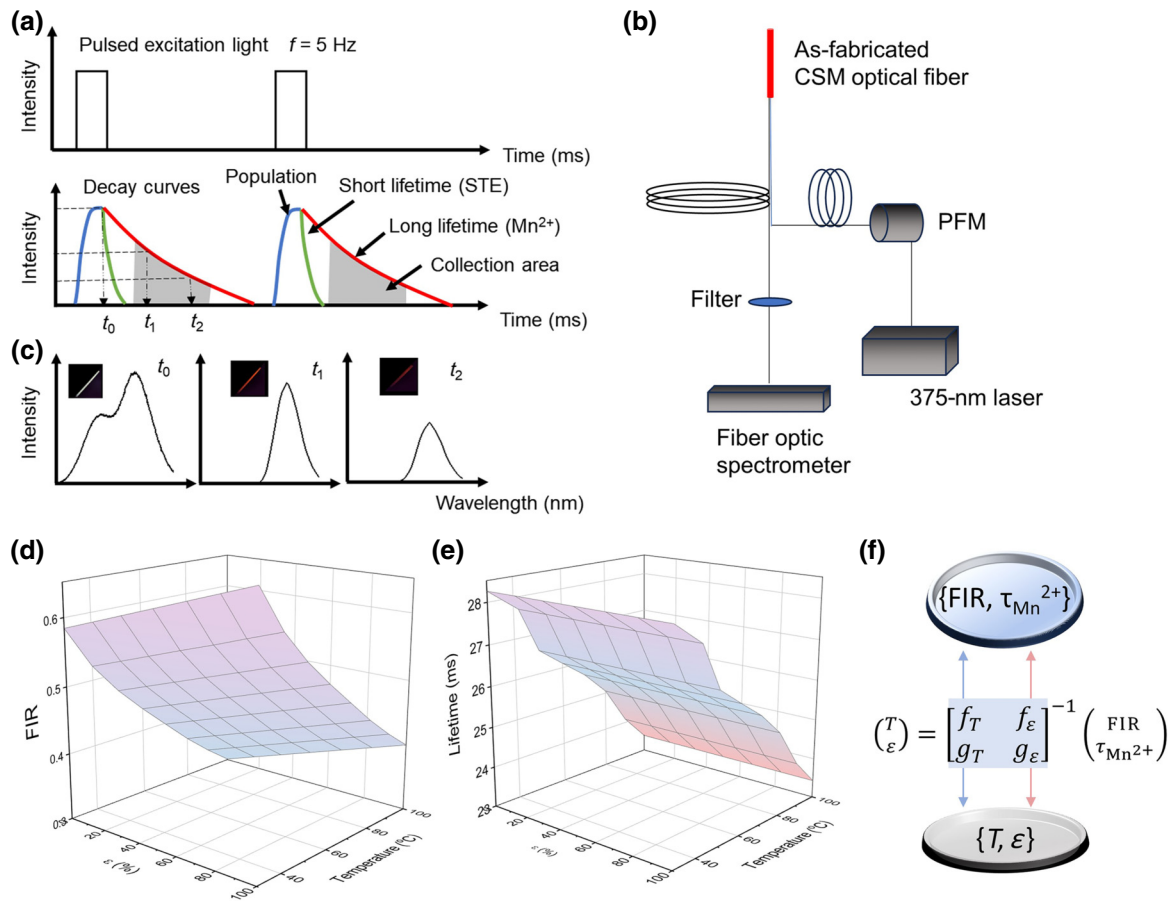


FIG. 3. Decoupling of the temperature and train sensing through the CSM optical fiber. (a) Schematic diagram of the decay time detection. (b) Diagrammatic depiction of the *in situ* detecting decay time of Mn²⁺ based on fiber optic spectrometer. (c) Transient spectra at time t_0 , t_1 , and t_2 , with an inset showing the corresponding luminescence photographs of the CSM fiber. (d) FIR values at various temperatures and strain. (e) Decay times at various temperatures and strains. (f) Collaborative sensing of the temperature and strain through the decoupling matrix via FIR and $\tau_{\text{Mn}^{2+}}$.

Since $\tau_{\text{Mn}^{2+}}$ is independent of strain, it can be concluded that $g_\varepsilon = 0$. As analyzed in Eqs. (S3)–(S7) in the Supplemental Material [24], the decoupling matrix can be defined as

$$\begin{bmatrix} f_T & f_\varepsilon \\ g_T & g_\varepsilon \end{bmatrix} = \begin{bmatrix} -\frac{4.65}{T} + 0.065 - 0.0002T + 2.73 \times 10^{-7}T^2 & 9.974 \times 10^{-4} \\ \frac{120.39}{T} - 0.65 + 0.0016T - 1.34 \times 10^{-6}T^2 & 0 \end{bmatrix}. \quad (18)$$

Consequently, the multisensory on temperature and strain can be realized by the CSM optical fiber based on FIR and $\tau_{\text{Mn}^{2+}}$.

VIII. CONCLUSION

In summary, we have designed various Mn²⁺-doped 0D LMH Rb₃KCdCl₆:0.2Sb crystals that display two distinct emissions derived from extrinsic STEs of Sb³⁺ (518 nm)

and $d-d$ transition of Mn²⁺ (605 nm). The efficient energy transfer from STE to Mn²⁺ centers was achieved and, thus, the tunable emission colors from green to orange were realized by varying the concentration of Mn²⁺ and the temperature. Based on the various responses of the two emissions, the FIR method can be employed to monitor the alterations; the maximum S_A , maximum S_R , and minimum δT are 0.011 K⁻¹ at 300 K, 5.22% K⁻¹ at 390 K, and 0.006 K at 390 K, respectively. Moreover,

owing to the isolated octahedron structure, the Mn^{2+} ions exhibited long decay times for tens of milliseconds, which is correlated to temperature while independent of strain. The as-prepared stretchable optical fiber was capable of detecting the temperature and strain with outstanding precision and repeatability. More importantly, the decoupling of temperature and strain sensing can be achieved by the matrix established by the FIR and the decay time of Mn^{2+} . This work paves the way for doped 0D luminescent metal halide with multiple emissions applied in multi-functional optical sensors, expanding their applications in sensing technology. Moreover, it provides a solution for decoupling the crosstalk on the multisensory so that reliability and practicality are enhanced.

ACKNOWLEDGMENTS

This research was supported by the National Natural Science Foundation of China (Grant no. 52302177) and the Guangdong Basic and Applied Basic Research Foundation (Grant no. 2024A1515011070).

- [1] D. Wencel, A. Kaworek, T. Able, V. Efremov, A. Bradford, D. Carthy, G. Coady, R. C. N. McMorrow, and C. McDonagh, Optical sensor for real-time pH monitoring in human tissue, *Small* **14**, e1803627 (2018).
- [2] H. Liang, Y. He, M. Chen, L. Jiang, Z. Zhang, X. Heng, L. Yang, Y. Hao, X. Wei, J. Gan, and Z. Yang, Self-powered stretchable mechanoluminescent optical fiber strain sensor, *Adv. Intell. Syst.* **3**, 2100035 (2021).
- [3] T. Xia, L. Jiang, J. Zhang, Y. Wan, Y. Yang, J. Gan, Y. Cui, Z. Yang, and G. Qian, A fluorometric metal-organic framework oxygen sensor: from sensitive powder to portable optical fiber device, *Microporous Mesoporous Mater.* **305**, 110396 (2020).
- [4] E. Song, M. Chen, Z. Chen, Y. Zhou, W. Zhou, H. T. Sun, X. Yang, J. Gan, S. Ye, and Q. Zhang, Mn^{2+} -activated dual-wavelength emitting materials toward wearable optical fibre temperature sensor, *Nat. Commun.* **13**, 2166 (2022).
- [5] W. Zhang, X. Huang, W. Liu, Z. Gao, L. Zhong, Y. Qin, B. Li, and J. Li, Semiconductor plasmon enhanced upconversion toward a flexible temperature sensor, *ACS Appl. Mater. Interfaces* **15**, 4469 (2023).
- [6] C. D. S. Brites, R. Marin, M. Suta, A. N. Carneiro Neto, E. Ximenes, D. Jaque, and L. D. Carlos, Spotlight on luminescence thermometry: basics, challenges, and cutting-edge applications, *Adv. Mater.* **35**, 2302749 (2023).
- [7] J. Liao, M. Wang, F. Lin, Z. Han, B. Fu, D. Tu, X. Chen, B. Qiu, and H.-R. Wen, Thermally boosted upconversion and downshifting luminescence in $Sc_2(MoO_4)_3$: Yb/Er with two-dimensional negative thermal expansion, *Nat. Commun.* **13**, 2090 (2022).
- [8] T. P. van Swieten, J. M. Steenhoff, A. Vlasblom, R. de Berg, S. P. Mattern, F. T. Rabouw, M. Suta, and A. Meijerink, Extending the dynamic temperature range of Boltzmann thermometers, *Light: Sci. Appl.* **11**, 343 (2022).
- [9] S. Yakunin, B. M. Benin, Y. Shynkarenko, O. Nazarenko, M. I. Bodnarchuk, D. N. Dirin, C. Hofer, S. Cattaneo, and M. V. Kovalenko, High-resolution remote thermometry and thermography using luminescent low-dimensional tin-halide perovskites, *Nat. Mater.* **18**, 846 (2019).
- [10] D. Liang, H. Xiao, W. Cai, S. Lu, S. Zhao, Z. Zang, and L. Xie, Mn^{2+} -based luminescent metal halides: syntheses, properties, and applications, *Adv. Opt. Mater.* **11**, 2202997 (2023).
- [11] S. Wang, S. Feng, R. Li, J. Jin, J. Wu, W. Zheng, Z. Xia, X. Chen, Q. Ling, and Z. Lin, Multiexciton generation from a 2D organic-inorganic hybrid perovskite with nearly 200% quantum yield of red phosphorescence, *Adv. Mater.* **35**, e2211992 (2023).
- [12] Z. Zhang, Light-emitting materials for wearable electronics, *Nat. Rev. Mater.* **7**, 839 (2022).
- [13] K. Hong, Q. V. Le, S. Y. Kim, and H. W. Jang, Low-dimensional halide perovskites: review and issues, *J. Mater. Chem. C* **6**, 2189 (2018).
- [14] M. Li and Z. Xia, Recent progress of zero-dimensional luminescent metal halides, *Chem. Soc. Rev.* **50**, 2626 (2021).
- [15] L. Sun, B. Dong, J. Sun, Y. Wang, R. Sun, S. Hu, B. Zhou, W. Xu, X. Bai, L. Xu, D. Zhou, and H. Song, Fabrication, optical property, and white LED application of novel lanthanide-based family Cs_2NaLnX_6 ($X = Cl, Br, I$) perovskite nanomaterials, *Laser Photonics Rev.* **17**, 2300045 (2023).
- [16] M. D. Smith and H. I. Karunadasa, White-light emission from layered halide perovskites, *Acc. Chem. Res.* **51**, 619 (2018).
- [17] F. Jiang, Z. Wu, M. Lu, Y. Gao, X. Li, X. Bai, Y. Ji, and Y. Zhang, Broadband emission origin in metal halide perovskites: are self-trapped excitons or ions?, *Adv. Mater.* **35**, 2211088 (2023).
- [18] J. Wang, Y. Yuan, C. Liu, R. Fu, L. Wang, F. Zhang, L. Ma, S. Jiang, Z. Shi, and H. Guo, Pressure-induced emission enhancement with an abnormal blue shift of the Sb^{3+} -doped zero-dimensional lead-free halide perovskite $Cs_2InBr_5 \cdot H_2O$, *Phys. Rev. B* **107**, 214111 (2023).
- [19] M. Cong, Q. Zhang, B. Yang, J. Chen, J. Xiao, D. Zheng, T. Zheng, R. Zhang, G. Qing, C. Zhang, and K. L. Han, Bright triplet self-trapped excitons to dopant energy transfer in halide double-perovskite nanocrystals, *Nano Lett.* **21**, 8671 (2021).
- [20] J. Jin, Y. Peng, Y. Xu, K. Han, A. Zhang, X.-B. Yang, and Z. Xia, Bright green emission from self-trapped excitons triggered by Sb^{3+} Doping in Rb_4CdCl_6 , *Chem. Mater.* **34**, 5717 (2022).
- [21] W. Zhang, J. Wei, Z. Gong, P. Huang, J. Xu, R. Li, S. Yu, X. Cheng, W. Zheng, and X. Chen, Unveiling the excited-state dynamics of Mn^{2+} in 0D Cs_4PbCl_6 perovskite nanocrystals, *Adv. Sci.* **7**, 2002210 (2020).
- [22] A. Zhang, J. Jin, and Z. Xia, Tunable luminescence of Sb^{3+} doped 0D Cs_4PbCl_6 nanocrystals from three distinct emission centers, *Adv. Opt. Mater.* **10**, 2200720 (2022).
- [23] Y. Qiu, Z. Ma, G. Dai, X. Fu, Y. Wang, X. Jia, and Z. Ma, Doped 0D Cs_4PbCl_6 single crystals featuring full-visible-region colorful luminescence, *J. Mater. Chem. C* **10**, 6227 (2022).

- [24] See Supplemental Material at <http://link.aps.org/supplemental/10.1103/PhysRevApplied.21.064054> for additional figures in support of the data analysis.
- [25] Z. Liu, Y. Pan, C. Peng, Y. Ding, H. Lian, J. Lin, and L. Li, Enhancing luminescence in Hue-tunable white-light emitting K₄CdCl₆:Sb³⁺, Mn²⁺ all-inorganic halide perovskites: insights from defect engineering and energy transfer, *ACS Appl. Mater. Interfaces* **15**, 51462 (2023).
- [26] D. L. Dexter, A theory of sensitized luminescence in solids, *J. Chem. Phys.* **21**, 836 (1953).
- [27] M. Pollnau, D. R. Gamelin, S. R. Lüthi, H. U. Güdel, and M. P. Hehlen, Power dependence of upconversion luminescence in lanthanide and transition-metal-ion systems, *Phys. Rev. B* **61**, 3337 (2023).
- [28] L. Peng, C. Wang, L. Li, F. Qin, Z. Zhang, *et al.*, Ratiometric optical thermometry based on upconversion luminescence with different multi-photon processes in CaWO₄:Tm³⁺/Yb³⁺ phosphor, *Opt. Lett.* **47**, 478285 (2022).
- [29] V. Trannoy, A. N. Carneiro Neto, C. D. S. Brites, L. D. Carlos, and H. Serier-Brault, Engineering of mixed Eu³⁺/Tb³⁺ metal-organic frameworks luminescent thermometers with tunable sensitivity, *Adv. Opt. Mater.* **9**, 2001938 (2021).
- [30] T. Zheng, L. Luo, P. Du, S. Lis, U. R. Rodríguez-Mendoza, V. Lavín, and M. Runowski, Highly-efficient double perovskite Mn⁴⁺-activated Gd₂ZnTiO₆ phosphors: A bifunctional optical sensing platform for luminescence thermometry and manometry, *Chem. Eng. J.* **446**, 136839 (2022).
- [31] X. Yuan, S. Ji, M. C. De Siena, L. Fei, Z. Zhao, Y. Wang, H. Li, J. Zhao, and D. R. Gamelin, Photoluminescence temperature dependence, dynamics, and quantum efficiencies in Mn²⁺-doped CsPbCl₃ perovskite nanocrystals with varied dopant concentration, *Chem. Mater.* **29**, 8003 (2017).
- [32] G. Zhang, P. Dang, L. Tian, W. Yang, Z. Cheng, H. Lian, and J. Lin, Boosting energy transfer from self-trapped exciton to Er³⁺ through Sb³⁺ doping in Cs₂Na(Lu/Er)Cl₆ double perovskites, *Adv. Opt. Mater.* **11**, 2202369 (2022).
- [33] Z. Rao, Z. Li, X. Zhao, and X. Gong, Targeted high-precision up-converting thermometer platform over multiple temperature zones with Er³⁺, *Mater. Horiz.* **10**, 1816 (2023).
- [34] M. Zheng, L. Li, D. Tian, Z. Zhang, W. Zhou, and M. He, Tailoring dye emissions within metal-organic frameworks for tunable luminescence and ratiometric temperature sensing, *ACS Appl. Mater. Interfaces* **15**, 23479 (2023).
- [35] D. Escofet-martin, A. O. Ojo, and B. Peterson, Ultrafast multi-phonon excitation of ScVO₄:Bi³⁺ for luminescence thermometry, *Opt. Lett.* **47**, 13 (2022).
- [36] M. D. Dramićannin, Ł. Marciniak, S. Kuzman, W. Piotrowski, Z. Ristić, J. Periša, I. Evans, J. Mitrić, V. Đorđević, N. Romčević, M. G. Brik, and C. Ma, Mn⁵⁺-activated Ca₆Ba(PO₄)₄O near-infrared phosphor and its application in luminescence thermometry, *Light: Sci. Appl.* **11**, 279 (2022).
- [37] X. Wang, F. Jahanbazi, J. Wei, C. U. Segre, W. Chen, and Y. Mao, Charge transfer-triggered Bi³⁺ near-infrared emission in Y₂Ti₂O₇ for dual-mode temperature sensing, *ACS Appl. Mater. Interfaces* **14**, 36834 (2022).
- [38] T. P. Swieten, D. Yu, T. Yu, S. J. W. Vonk, M. Suta, Q. Zhang, A. Meijerink, and F. T. Rabouw, A Ho³⁺-based luminescent thermometer for sensitive sensing over a wide temperature range, *Adv. Opt. Mater.* **9**, 2001518 (2021).
- [39] W. Cao, Y. Cui, Y. Yang, and G. Qian, Dyes encapsulated nanoscale metal-organic frameworks for multimode temperature sensing with high spatial resolution, *ACS Mater. Lett.* **3**, 1426 (2021).
- [40] G.-S. Zheng, C.-L. Shen, Q. Lou, J.-F. Han, Z.-Z. Ding, Y. Deng, M.-Y. Wu, K.-K. Liu, J.-H. Zang, L. Dong, and C.-X. Shan, Meter-scale chemiluminescent carbon nanodot films for temperature imaging, *Mater. Horiz.* **9**, 2533 (2022).
- [41] H. Yu, Y. Tan, and B. T. Cunningham, Smartphone fluorescence spectroscopy, *Anal. Chem.* **86**, 8805 (2014).
- [42] S. Li, J. Luo, J. Liu, and J. Tang, Self-trapped excitons in all-inorganic halide perovskites: fundamentals, status, and potential applications, *J. Phys. Chem. Lett.* **10**, 1999 (2019).
- [43] M. Chen, Y. He, H. Liang, H. Zhou, X. Wang, X. Heng, Z. Zhang, J. Gan, and Z. Yang, Stretchable and strain-decoupled fluorescent optical fiber sensor for body temperature and movement monitoring, *ACS Photonics* **9**, 1415 (2022).
- [44] C. Shang, B. Fu, J. Tuo, X. Guo, Z. Li, Z. Wang, L. Xu, and J. Guo, Soft biomimetic fiber-optic tactile sensors capable of discriminating temperature and pressure, *ACS Appl. Mater. Interfaces* **15**, 53264 (2023).
- [45] C. Hou, H. Wang, Q. Zhang, Y. Li, and M. Zhu, Highly conductive, flexible, and compressible all-graphene passive electronic skin for sensing human touch, *Adv. Mater.* **26**, 5018 (2014).